# Termination of pinned vortices by high-frequency wave trains in heartlike excitable media with anisotropic fiber orientation

Marcel Hörning[1,2,*]
[1]*Department of Physics, Graduate School of Science, Kyoto University, Japan*
[2]*Laboratory for Physical Biology, RIKEN Center for Developmental Biology, Kobe, Japan*
(Received 12 June 2012; revised manuscript received 22 July 2012; published 14 September 2012)

A variety of chemical and biological nonlinear excitable media, including heart tissue, exhibit vortices (spiral waves) that can anchor to nonexcitable obstacles. Such anchored vortices can be terminated by the application of high-frequency wave trains, as shown previously in isotropic excitable media. In this study, we examined the basic dependencies of the conduction velocities of planar waves and waves around curved obstacles as a function of anisotropy through numerical simulations of excitable media that mimic the fiber orientation in a real heart. We also investigated the unpinning of anchored spiral waves by high-frequency wave trains in an anisotropic excitable medium. Unlike the findings regarding the termination of spiral waves in isotropic excitable systems, we found a nonmonotonic relationship between the maximum unpinning period and the obstacle radius depending on the fiber orientation, where the formation of unwanted secondary pinned vortices or chaotic waves is seen over a wide range of parameters.

DOI: 10.1103/PhysRevE.86.031912 PACS number(s): 87.18.Hf, 05.45.−a, 87.19.Hh

## I. INTRODUCTION

Cardiac arrhythmias represent a life-threatening heart condition [1–3]. A large class of arrhythmias are associated with single or multiple reentries (spiral waves) that may rotate freely or may become anchored at anatomical obstacles, such as blood vessels and scars [4–7]. Anchored spiral waves may be resistant to antitachycardia pacing (ATP) [8–14], a high-frequency pacing therapy that is applied through an implantable cardioverter defibrillator [15,16].

An alternative to clinically used ATP therapy is the application of low-energy antifibrillation pacing (LEAP), which engages excitable tissue around heterogeneities in the heart without physical contact [17]. Recently, both theoretical and experimental studies have demonstrated the success of this approach in terminating single spiral waves [18,19] and fibrillation-like states (spatiotemporal chaos) [20,21]. Various underlying mechanisms have been proposed [17,20,22–25] in an attempt to advance the methodology so that it can be used clinically.

Despite recent progress in the application of ATP and LEAP therapy, much remains to be understood regarding the dynamics of spiral waves and their termination in real heart tissue. Most experimental (*in vitro*) and theoretical studies that have investigated the formation and termination of spiral waves in excitable tissue have oversimplified essential structural features of the heart that set it apart from other excitable systems. Specifically, the cell anisotropy and complex fiber orientation that define the nonlinear effects of wave propagation in the heart [26,27] are typically ignored in a consideration of isotropic excitable media [8,9,12–14,18–20,23].

In this study, we used numerical simulations to investigate some basic relations of wave propagation in excitable tissue that exhibits cellular anisotropy and fiber orientation. We found that there is a strong correlation between the conduction velocity (CV) of single waves ($c_{\mathrm{sin}}$) and the critical CV of high-frequency entrained waves ($c_{\mathrm{crit}}$) that lead to wave failure of planar waves or unpinning of waves around curved obstacles. We found a linear relationship between $c_{\mathrm{sin}}$ and $c_{\mathrm{crit}}$ for both types of waves. However, planar waves show no dependence on the level of cellular anisotropy.

Further, we derived a simple relationship that has the form of an eikonal equation by introducing an effective diffusion $D_{\mathrm{eff}}$ to a system that exhibits anisotropic diffusivity. With knowledge obtained regarding the dependence of CV on round obstacles, we illustrate the effect of cellular anisotropy on the termination of spiral waves that are pinned to obstacles. We found a nonmonotonic dependence between the obstacle radius, the cellular anisotropy ratio, and the maximum unpinning period, in contrast to previous results in isotropic excitable medium [12] and in electroelastic excitable medium [13]. Further, we found that for a wide range of parameters, high-frequency wave trains can induce undesirable secondary pinned spiral waves at obstacles or even promote chaoslike wave behavior. These findings are important when considering the safety of this therapy for cardiac arrhythmias.

## II. NUMERICAL METHODS

In this study, we performed numerical simulations with the simplified ionic model of heart tissue described by Fenton and Karma [28]. This model captures the essential features of cellular dynamics and can reproduce a range of physiological behavior in the heart [8,12,29–31].

A two-dimensional slab of continuous cardiac tissue with cellular anisotropy is considered. The basic equation for the membrane potential $\mathbf{V}$ is

$$\partial_t \mathbf{V} = \nabla \cdot (\mathbf{D}\nabla \mathbf{V}) - J_{\mathrm{ion}}(\mathbf{V};\mathbf{v};\mathbf{w})/C_{\mathrm{m}}, \tag{1}$$

where $\mathbf{D}$ is the diffusion tensor, $C_m$ is the membrane capacity, and $J_{\mathrm{ion}}$ is the sum of the three main currents. The membrane potential $\mathbf{V}$ and currents $J_{\mathrm{fi}}$, $J_{\mathrm{si}}$, and $J_{\mathrm{so}}$ are scaled by definition to the dimensionless variables $u \equiv (V - V_o)/(V_{\mathrm{fi}} - V_o)$ and

*Author to whom all correspondence should be addressed: marcel@cdb.riken.jp

 

$I \equiv J/[C_m(V_{\rm fi} - V_o)]$, respectively, where $V_{\rm fi}$ is the Nernst potential of the fast inward current and $V_o$ is the resting membrane potential. If we make the substitution $u_s = u - u_c$, where $u_c$ is a parameter, the model equations are

$$\partial_t u = \mathbf{D}\nabla \cdot (\nabla \mathbf{u}) - I_{\rm fi}(u;v) - I_{\rm si}(u;w) - I_{\rm so}(u), \quad (2)$$

$$\partial_t v = \Theta(-u_s)(1-v)/\tau_v^-(u) - \Theta(u_s)\, v/\tau_v^+, \quad (3)$$

$$\partial_t w = \Theta(-u_s)(1-w)/\tau_w^- - \Theta(u_s)\, w/\tau_w^+, \quad (4)$$

with

$$\tau_v^-(u) = \left[\Theta(u-u_v)\,\tau_{v1}^- + \Theta(u_v-u)\,\tau_{v2}^-\right], \quad (5)$$

and the currents are defined as

$$I_{\rm fi} = -\frac{v}{\tau_d}\Theta(u_s)(1-u)(u_s), \quad (6)$$

$$I_{\rm si} = \frac{u}{\tau_o}\Theta(-u_s) + \frac{1}{\tau_r}\Theta(u_s), \quad (7)$$

$$I_{\rm so} = -\frac{w}{2\tau_{\rm si}}\left\{1 + \tanh\left[k\left(u - u_c^{\rm si}\right)\right]\right\}, \quad (8)$$

where $\Theta(x)$ is the Heaviside step function

$$\Theta(x) = \begin{cases} 1 & \text{if } x \geqslant 0, \\ 0 & \text{otherwise} \end{cases} \quad (9)$$

and

$$\tau_d = C_m/g_{\rm fi} \quad (10)$$

is a time constant that regulates depolarization on the membrane. A two-dimensional symmetric diffusion tensor $\mathbf{D}$ is introduced as

$$\mathbf{D} \equiv \begin{pmatrix} D_{\rm x} & D_{\rm xy} \\ D_{\rm xy} & D_{\rm y} \end{pmatrix} \quad (11)$$

with

$$D_{\rm y} = D_\parallel \cos^2\Phi + D_\perp \sin^2\Phi, \quad (12)$$

$$D_{\rm x} = D_\parallel \sin^2\Phi + D_\perp \cos^2\Phi, \quad (13)$$

$$D_{\rm xy} = (D_\parallel - D_\perp)\cos^2\Phi \sin^2\Phi, \quad (14)$$

where $D_\parallel$ and $D_\perp$ are the diffusivities for propagation parallel and perpendicular to the fiber direction, respectively, and $\Phi$ is the inclination angle of the fiber in the plane with respect to the horizontal axis. The parameters were chosen from the modified Beeler-Reuter (MBR) variable set in the original article by Fenton and Karma [28]. The depolarization parameter, $g_{\rm fi}$, was set to 2.40 mmho/cm$^2$ while time and spatial discretization were set to $dt = 0.02$ ms and $dx = 0.016$ cm, respectively. The parallel diffusivity was set to $D_\parallel = 1 \times 10^{-3}$ cm$^2$/ms and $D_\perp$ was changed by defining the anisotropy ratio to $d_r = D_\parallel/D_\perp$. The value of $d_r$ was varied between 1 and 10, based on a consideration of values that have been observed in experiments on heart tissue [32–34]. In the case of $d_r = 1$, the diffusivities become equal and the system is isotropic. Equation (2) is solved by using a two-dimensional alternating-direction implicit scheme [28,35], while Eqs. (3) and (4) are integrated exactly from $n\Delta t$ to time $(n+1)\Delta t$ according to the general solutions

$$y_\alpha^{n+1} = y_\alpha^n e^{-\Delta t/\tau_y^+} \quad (15)$$

and

$$y_\alpha^{n+1} = 1 - \left[1 - y_\alpha^n\right]e^{-\Delta t/\tau_y^-} \quad (16)$$

when $u > u_v$ and $u < u_v$, respectively.

To simulate nonconductive tissue, an area in the tissue was disconnected electrically following the basic concept of the phase-field method, where a spatially diffuse interface of finite thickness is defined [36].

The trajectories of wave tips are obtained by defining the intersection of a single isopotential line with a constant membrane potential, $V(\mathbf{r},t) = V_{\rm iso}$ with $u_{\rm iso} \equiv (V_{\rm iso} - V_o)/(V_{\rm fi} - V_o)$, and the point of zero normal velocity $c(\mathbf{r},t) = 0$, where $\mathbf{r}$ is the position vector. $V_{\rm iso}$ is chosen to be $-35$ mV corresponding to $u_{\rm iso} = 0.5$, which represents the boundary between depolarization and repolarization in the tissue [28,31].

## III. RESULTS

To understand the mechanism of the unpinning of spiral waves from anchored nonexcitable obstacles in realistic excitable media, we studied the effect of wave propagation in anisotropic media in more detail. To demonstrate the effect of anisotropy on the conduction of spreading waves, examples of free rotating spiral waves and single-stimulus-induced target patterns in isotropic and anisotropic excitable media are shown in Fig. 1. Spiral waves in isotropic ($d_r = 1$) and anisotropic ($d_r = 5$) media are shown in Figs. 1(a) and 1(b), respectively. The anisotropic diffusion in Fig. 1(b) with a fiber rotation angle of $\Theta = 45^\circ$ leads to the elongation of spiral propagation parallel to the direction of higher conductivity. This leads to a

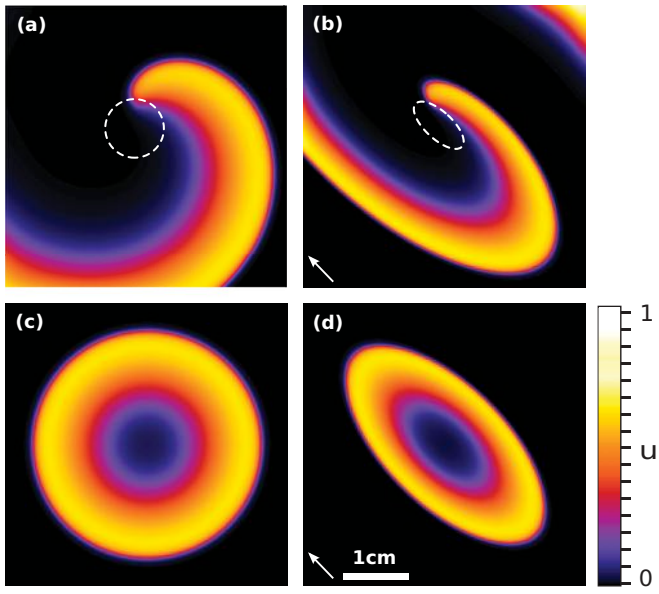


FIG. 1. (Color online) Examples of pattern formation in isotropic and anisotropic excitable media. (a) and (b) show free spiral waves, and (c) and (d) target waves that originate at the center of the media. (a) and (c) show wave propagation in isotropic media ($d_r = 1$), and (b) and (d) show wave propagation in anisotropic media ($d_r = 5$) with a fiber rotation angle of $\Phi = 45^\circ$. The white arrows indicate the main fiber orientation. The wave-tip trajectory of spiral waves is illustrated with white dashed lines and shows a closed circle and an oval loop, respectively, which is due to the choice of parameters.

difference in the CV parallel and perpendicular to the axis of fiber rotation, which further deforms the spiral tip trajectory, as illustrated by the white dashed line shown in Fig. 1(b). For comparison, the isotropic case of a free rotating spiral wave leads to a round spiral tip trajectory [Fig. 1(a)]. Other spiral trajectories, such as petal-like shapes, are also possible depending on the choice of parameters [28]. Target waves show similar features, as illustrated in Figs. 1(c) and 1(d), respectively. Generally, the CV is related to the strength of cell-to-cell coupling [see Eq. (1)] and the characteristics of the action potential upstroke [27], and thus an increase in the rate of anisotropy ($d_r$) leads to an increase in CV perpendicular to the axis of fiber rotation when CV parallel is held constant.

### A. Conduction velocity of planar wave trains

First, we reinvestigate some properties of the CV of planar waves as a function of fiber orientation, considering that our main aim is to understand the underlying dynamics of wave propagation along curved obstacles. Here, we define the fiber rotation angle $\Phi$ with respect to the direction of the plane wave. Generally, CV depends on $\Phi$. If $\Phi = 0^\circ$, which defines the wave propagation along $D_\parallel$ [see Eq. (11)], the wave propagates faster than for $\Phi = 90^\circ$, which corresponds to propagation along $D_\perp$. Thus, the restitution curves depend on $\Phi$, as shown in Fig. 2(a) for an anisotropy ratio of $d_r = 5$ for $\Phi$ equal to $0^\circ$, $30^\circ$, $60^\circ$, and $90^\circ$. The restitution curves are obtained

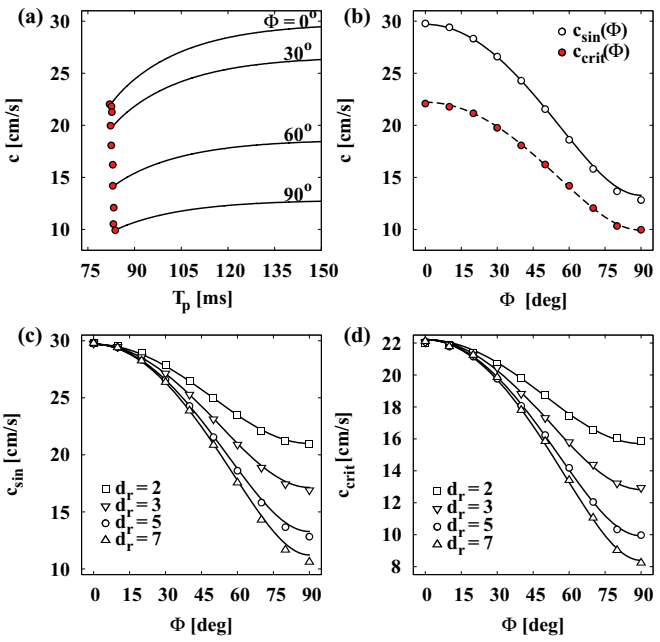


FIG. 2. (Color online) Plane wave propagation in anisotropic excitable media. (a) shows the restitution curves for waves in the direction $\Phi = 0^\circ$, $30^\circ$, $60^\circ$, and $90^\circ$ with respect to the fiber orientation for an anisotropy ratio of $d_r = 5$. $T_{\text{crit}}$ is shown as red data points for $\Phi$ in steps of $10^\circ$. Corresponding $c_{\text{sin}}$ and $c_{\text{crit}}$ are shown in (b). The black solid line shows the analytic solution of $c_{\text{sin}}(\Phi)$ according to Eq. (19), and the black dashed line shows the estimation of $c_{\text{crit}}(\Phi)$ according to Eq. (20) with $\lambda_{\text{pw}} = 0.75$. (c) and (d) show $c_{\text{sin}}$ and $c_{\text{crit}}$, respectively, similar to (b) for different $\Phi$. The black dashed lines in (d) illustrate Eq. (20) with $\lambda_{\text{pw}} = 0.75$. Thus, $\lambda_{\text{pw}}$ is shown to be an independent function of $d_r$ for plane propagating waves.

measuring the propagation time at a distance of 150 pixels (2.4 cm) by the dynamical pacing scheme, as introduced by Hörning *et al.* [12], to minimize the initial alternating effect of periodically paced waves [37,38]. The pacing period $T_p$ can be defined as a dynamical decreasing step function

$$T_p^n = T_p^{n-1} - \Theta(n - a_s)T_d, \tag{17}$$

where $T_p^0$ is the initial period $T_0$, $T_d$ is the discrete step of change in the period per iteration, which is set to be 0.1 ms for the investigation of the CVs and 1.0 ms for investigations on the termination of vortices, $n$ is the number of applied stimuli, and $a_s$ is a sequence defined as

$$a_s = ps \qquad (s \in \mathbb{N}) \tag{18}$$

with $p = 3$, and $s$ is defined in the interval $[0 : \infty]$. This corresponds to a stimulation protocol of three consecutive, constant applied stimuli that decrease in steps of $T_d$. Thus, only every third applied stimulus is used to reproduce the restitution curves shown in Fig. 2(a). The critical pacing period $T_{\text{crit}}$ is obtained when a wave fails to propagate, leading to a 2 : 1 type of Wenckebach rhythm [39]. The red data points in Fig. 2(a) show $T_{\text{crit}}$ for every $10^\circ$ of fiber rotation. As expected, we find that $T_{\text{crit}}$ can be considered to be independent of $\Phi$, leading to an average $T_{\text{crit}}$ of $82.8 \pm 0.5$ ms.

The CV of a single plane wave, $c_{\text{sin}}$, that is propagating in a recovered medium corresponds to a pacing period of $T \to \infty$, and the $c_{\text{crit}}$ corresponds to a plane wave that is stimulated with $T_{\text{crit}}$. Thus, we can show that CV is a function of $\Phi$. Figure 2(b) shows $c_{\text{sin}}$ and $c_{\text{crit}}$ as white and red data points, respectively. Both dependencies decrease monotonically for an increase in $\Phi$ following the analytic obtained relation

$$c(\Phi) = c_{\Phi=0^\circ}\sqrt{\cos^2\Phi + d_r^{-1}\sin^2\Phi}, \tag{19}$$

see, e.g., Keener and Sneyd [40]. Further, $c_{\text{crit}}$ can be expressed as

$$c_{\text{crit}} = \lambda_{\text{pw}} c_{\text{sin}}, \tag{20}$$

where $\lambda_{\text{pw}}$ is a constant which is defined as the ratio between $c_{\text{crit}}$ and $c_{\text{sin}}$ for plane waves. The black dashed line shown in Fig. 2(b) shows the validity of Eqs. (19) and (20), where $\lambda_{\text{pw}}$ is found to be 0.75. Moreover, $\lambda$ is an independent function of $d_r$, as shown in Figs. 2(c) and 2(d), which show $c_{\text{sin}}(d_r)$ and $c_{\text{crit}}(d_r)$ as a function of $\Phi$, similar to that shown in Fig. 2(b), respectively. The dashed lines in Fig. 2(d) show the approximation of Eq. (20) for $\lambda_{\text{pw}} = 0.75$.

### B. Conduction velocity on round obstacles

Next, we investigate waves that propagate around curved obstacles. We introduce a finger-shaped obstacle (see Fig. 3), and we restrict our investigation to the case of $\Phi = 0^\circ$ (parallel diffusivity) for simplicity. Waves originate on the top-right of the obstacle and propagate along the boundary of the obstacle. First, planar waves propagate with $c_l$, then decrease to $c_c$ on the curved part of the obstacle, and finally speed up to $c_l$ after the waves reach the planar region of the obstacle's lower part. Although $c_c$ depends on the position around the obstacle, since $\Phi$ changes with respect to the direction of normal wave propagation, we measure $c_c$ on the curved part of the obstacle

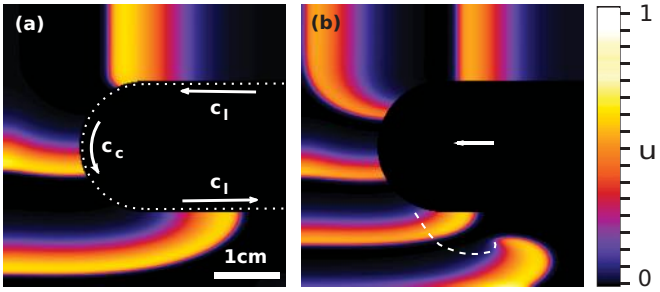


FIG. 3. (Color online) Example of wave propagation on finger-shaped obstacles. (a) and (b) show high-frequency paced wave propagation on a finger-shaped obstacle with a radius of 1 cm in an anisotropic medium ($d_r = 5$ and $\Phi = 0°$). The white arrow in (b) indicates the main fiber orientation. The obstacle contour is emphasized by a white dotted line in (a). Waves originate at the top right of the obstacles using a dynamic stimulation protocol [see Eq. (17)]. The pacing period $T_p(n)$ is 123.8 and 92.2 ms in (a) and (b), respectively. Arrows in (a) illustrate the change in CV from $c_l$ to $c_c$ and back to $c_l$ depending on the obstacle curvature. (b) shows a wave that detached from the obstacle. The wave tip is shown as a white dashed line from the time of detachment.

as the mean time the wave needs to propagate from the upper to the lower end of the curved obstacle following the basic equation

$$c_c = \pi R(dt_c)^{-1}, \tag{21}$$

where $R$ is the radius of the obstacle and $dt_c$ is the time duration the wave is propagating along the curvature of the obstacle. Thus, we can measure the average $c_c$ as a function of the curvature, $\kappa = R^{-1}$, $T_p$, and $d_r$. Figures 4(a) and 4(b) illustrate $c_{\sin}$ and $c_{\text{crit}}$ on obstacles with radii ranging from 0.25 to 1.5 cm, respectively, following the notation introduced for plane propagating waves. $c_{\text{crit}}$ is obtained when the propagating wave detaches from the obstacle, as shown in Fig. 3(b). We find that, in both cases, the relationship between CV and $\kappa$ can be expressed in a more general form of an eikonal equation,

$$c_c = c_0 - \kappa \frac{\partial c_c}{\partial \kappa}, \tag{22}$$

where $c_0$ is the interpolation of the $c_c$ to $\kappa = 0$, and $\frac{\partial c_c}{\partial \kappa}$ defines the slope with a dimension of a diffusion coefficient. Thus, we can simplify the right term in Eq. (22) to

$$\tilde{D} = \frac{\partial c_c}{\partial \kappa}, \tag{23}$$

which can be interpreted as an effective diffusion. By comparing the slopes of single and critical wave speeds, we find a relationship that is similar to the one we introduced earlier for plane waves [see Eq. (20)], except that the factor $\lambda_{\text{pw}}$ is now a function of $d_r$. Thus, we rewrite Eq. (20) to the more generalized form

$$c_{\text{crit}}(d_r,\kappa) = \lambda(d_r) c_{\sin}(d_r,\kappa). \tag{24}$$

Figure 4(c) shows a comparison of the slopes $\partial c/\partial \kappa$ obtained from the linear approximations illustrated in Figs. 4(a) and 4(b) (black solid lines) with white round and square data points, respectively. The black solid lines are arbitrary power-law functions that fit the two data sets best. Next, we introduce

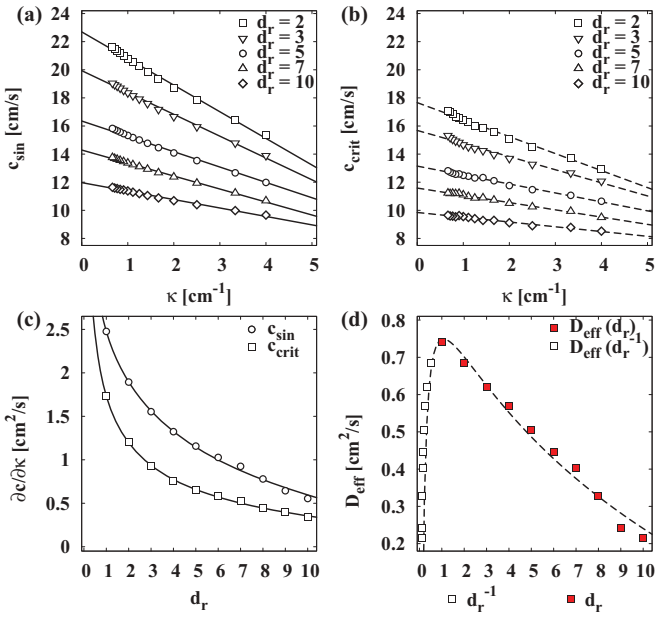


FIG. 4. (Color online) Conduction velocity on finger-shaped obstacles. (a) shows the CV of single propagating waves and (b) shows the critical CV of high-frequency paced waves as a function of the obstacle curvature for various $d_r$. The black solid and dashed lines in (a) and (b) show the respective linear approximations. (c) shows the slopes obtained from (a) and (b) for $c_{\sin}$ and $c_{\text{crit}}$ as round and square data points, respectively. The black solid lines show the best fit of arbitrary power-law functions with the powers $-0.04$ and $-0.36$, respectively. (d) illustrates the effective diffusivities ($D_{\text{eff}}$) following the relation in Eq. (26). The red and white squares show $D_{\text{eff}}$ as a function of $d_r$ and $d_r^{-1}$, respectively. The black dashed line shows Eq. (26) considering the power-law functions obtained in (c).

the effective diffusion $D_{\text{eff}}(d_r)$, which describes the rate of slowing from $c_{\sin}$ to $c_{\text{crit}}$ at a round obstacle with curvature $\kappa$, which satisfies the relation

$$c_{\text{crit}} = c_{\sin} - \kappa D_{\text{eff}}. \tag{25}$$

When we calculate the partial derivative with respect to $\kappa$ and consider Eq. (23), we obtain

$$D_{\text{eff}} = \tilde{D}_{\sin} - \tilde{D}_{\text{crit}}. \tag{26}$$

Figure 4(d) shows $D_{\text{eff}}$ as a function of $d_r$ with red squares. The white squares show $D_{\text{eff}}$ for values of $d_r$ smaller than 1, and they are obtained by considering $D_{\text{eff}}$ as a function of $d_r^{-1}$. The black dashed line shows Eq. (26) by considering the power-law functions obtained in Fig. 4(c). Both $D_{\text{eff}}(d_r)$ and $D_{\text{eff}}(d_r^{-1})$ represent the data well (see black dashed line). Thus, we can define Eq. (25) depending on $D_{\text{eff}}$, as a generic equation that determines $c_{\text{crit}}$ without knowledge of the wavefront curvature, which is necessary to define the classic eikonal equation in excitable media [41,42], or detailed information regarding parallel and perpendicular diffusivity.

### C. Termination of anchored vortices

Spiral waves that are anchored to a nonexcitable obstacle can be terminated in a manner similar to that shown above for wave propagation on finger-shaped obstacles. Waves that are propagating on obstacles need to be slowed down

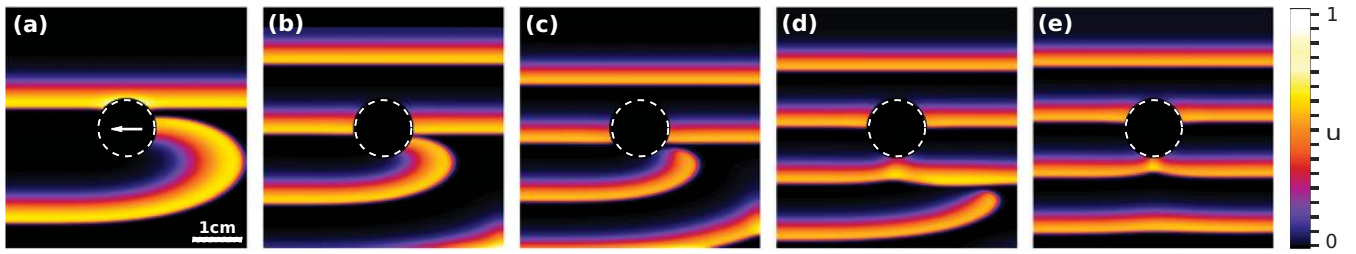


FIG. 5. (Color online) Termination of a pinned spiral wave in an anisotropic excitable medium by a high-frequency wave train. The obstacle radius is 0.6 cm, the fiber orientation is $\Phi = 0^\circ$, and the anisotropy ratio is $d_r = 5$. The white arrow in (a) indicates the main fiber orientation. Planar waves originate on the top. Snapshots are illustrated at pacing periods of 180, 114, 101, 98, and 97 ms, respectively, following the dynamic pacing protocol with an iteration period of 1 ms [see Eq. (17)]. The maximum unpinning period is 101 ms, as illustrated in (c), and subsequent approaching waves push the free spiral wave to the boundary of the system (d), where it finally terminates (e).

until local conduction block occurs [see Fig. 3(b)], which eventually leads to the termination of newly formed free spiral waves at the boundary of the system due to subsequently approaching waves. An increase in both the curvature and wave train frequency can promote the slowing down of waves on obstacles, as has been illustrated theoretically in isotropic excitable media [12]. The basic mechanism for the unpinning of an anchored spiral wave is consistent with that in anisotropic media, as illustrated in Fig. 5. If we consider that the pacing frequency is higher than the rotational frequency of a pinned spiral wave, the following basic scenario can be proposed. First, paced waves advance toward the obstacle [Fig. 5(a)] until the system entrains to a periodic pattern of annihilation between the approaching waves and the newly formed spiral wave at the obstacle [Fig. 5(b)]. When the CV of the pinned spiral wave finally reaches the critical CV, due to the interaction of the curvature of the wavefront on the obstacle [similar to that shown in Fig. 3(b)], local conduction block occurs at the tip of the spiral wave. This leads to displacement of the spiral tip apart from the obstacle [Fig. 5(c)]. Subsequent arriving waves push the free spiral wave away from the obstacle [Fig. 5(d)] and to the boundary of the system [Fig. 5(e)]. The latter part of this process, from when the spiral tip detaches from the obstacle, is reminiscent of the mechanism of the termination of weakly anchored spiral waves, which is discussed in detail in Pumir *et al.* [11].

In contrast to the monotonic functional dependence of the maximum unpinning period on the obstacle radius that is observed in isotropic excitable media [10,12,13], we found that the termination of spiral waves by high-frequency wave trains in anisotropic excitable media leads to nonmonotonic functional dependence for a certain range of $\Phi$. Figure 6(a) shows the dependence of the maximum unpinning period ($T_{\mathrm{unp}}$) as a function of fiber orientation ($\Phi$) for three different obstacle radii. Additionally, the critical pacing period of planar waves is shown as a black line for comparison. Smaller $\Phi$ leads to a similar monotonic dependence as observed in isotropic media. However, larger $\Phi$ leads to a nonmonotonic relationship between $R$ and $T_{\mathrm{unp}}$. Figure 6(b) shows this nonmonotonic behavior for $\Phi = 30^\circ$ and $70^\circ$ as red circles and blue squares, respectively. The corresponding values of $\Phi$ are highlighted as black dashed lines in Fig. 6(a). In the case of $\Phi = 70^\circ$, we observed an increase in $T_{\mathrm{unp}}$ for larger $R$ after a subsequent decrease in $T_{\mathrm{unp}}$ for smaller $R$.

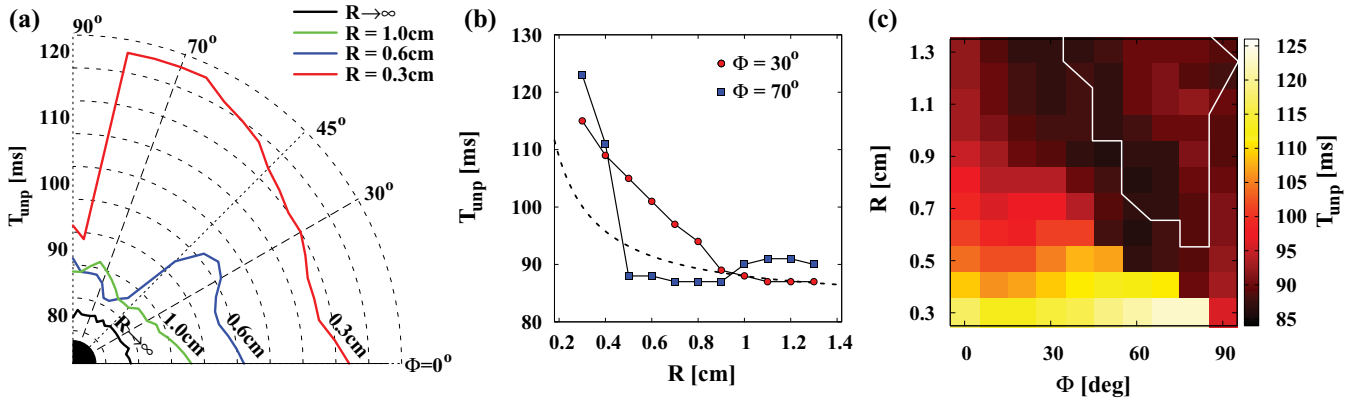


FIG. 6. (Color online) Maximum unpinning period from a round obstacle in anisotropic excitable media ($d_r = 5$). (a) shows the dependence of fiber orientation $\Phi$ and the maximum unpinning period $T_{\mathrm{unp}}$ for obstacle radii, $R$, of 0.3, 0.6, and 1.0 cm in red, blue, and green lines, respectively. The critical pacing period for planar waves ($R \to \infty$) is shown as a black line. (b) shows the the dependence of $R$ and $T_{\mathrm{unp}}$ for $\Phi = 30$ and $70^\circ$ as red data points and blue squares, respectively. The dashed black line shows the approximation of Eq. (27) for $\Phi = 30^\circ$ (see also Ref. [12]). The corresponding $\Phi$ are highlighted as black dashed lines in (a). (c) shows the dependence of $R$, $\Phi$, and the unpinning period $T_{\mathrm{unp}}$ as a heat map. The white solid line encircles the parameter space, where double-pinned spiral waves are formed temporarily before unpinning of the spiral wave or the development of chaotic wave formation.

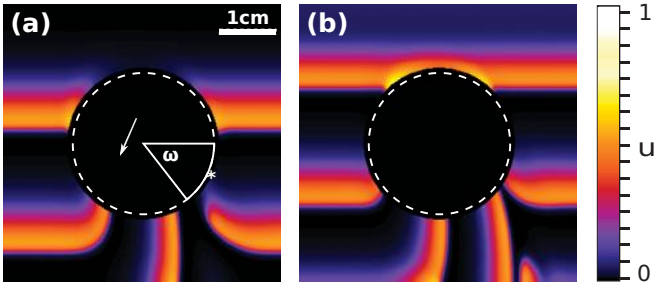


FIG. 7. (Color online) Secondary pinned spiral waves due to an asymmetric conduction block. The obstacle radius is 1.3 cm, the fiber orientation is $\Phi = 70^\circ$, and the anisotropy ratio is $d_r = 5$. The white arrow in (a) indicates the main fiber orientation. Planar waves originate on the top. (a) shows the obstacle-detached wave arm of the approaching planar waves due to local conduction block. In (b), the detached wave is pushed toward the boundary and two pinned spiral waves remain on the obstacle, which is consistent with a topological charge of $+2$. The pacing period in (a) and (b) is 89 and 87 ms, respectively. The circle segment $\omega$ in (a) identifies the window for the possible induction of multiple pinned spiral waves, and the asterisk shows the position of highest diffusivity on the obstacle within the range of curling waves (lower half of the obstacle). This example ($\Phi = 70^\circ$ and $R = 1.3$ cm) corresponds to the example shown in Fig. 6(b).

Figure 6(c) shows the dependence of $R$, $\Phi$, and the unpinning period $T_{\text{unp}}$ as a heat map. A sharp transition toward larger $T_{\text{unp}}$, as can be seen for $R = 0.3$ and 0.6 cm in Fig. 6(a) and $\Phi = 70^\circ$ in Fig. 6(b), is observed for large $\Phi$ on small obstacles, with damping tendency toward smaller $\Phi$ on obstacles with larger radii.

Further, we found that, for a certain parameter space encircled by the white solid line in Fig. 6(c), the unpinning scenario is different. The pinned spiral wave does not unpin from the obstacle, but rather from the wave that approaches the spiral wave from the opposite direction of the obstacle. Thus, a change in the topological charge (i.e., a sum of the individual chiralities on the obstacle [11,43]) from $+1$ (one pinned spiral) to $+2$ (two pinned spirals) at the obstacle can be observed temporarily before subsequent waves lead to the termination of the pinned spiral waves or the development of chaotic wave formation. We observed the latter only in rare cases, and they strongly depended on the distance between the obstacle and the boundary, and the type of spiral wave trajectory [7]. Figure 7 shows an example of the formation of temporary double-pinned spiral waves. This scenario can be explained by the relative orientation of the fibers at the obstacle. If the position of the highest diffusivity ($D_\parallel$) is before the position of the annihilation of the spiral wave and after the position on the obstacle when approaching waves start to curl (lower half of the obstacle), then the approaching waves will detach before the pinned spiral wave due to the sudden decrease in diffusivity from $D_\parallel$ to $D_\perp$ at the boundary of the obstacle. Figure 7 shows the circle segment $\omega$ of this region with solid white lines and the position of the highest diffusivity ($D_\parallel$) by an asterisk. However, the counterpart of the obstacle with mirroring diffusivities is unaffected, since the approaching waves do not curl in that region, but approach as plane waves. This explains the sharp transition in conventional unpinning [8,12,13] and the newly found re-initiation of a secondary spiral wave at $\Phi = 80^\circ$. When $\Phi = 90^\circ$, the position of the highest diffusivity ($D_\parallel$) falls on the boundary between the upper and lower sides of the obstacle, and thus the range of $\omega$ decreases virtually to zero, which is, however, necessary for the formation of double-pinned spiral waves.

Finally, we compare the validity of the theoretical framework that predicts the maximum unpinning period $T_{\text{unp}}$ in isotropic excitable media [12]. The basic equation is

$$T_{\text{unp}} = T_{\text{crit}} \left( 1 + \frac{D}{R(c_0 - c_{\text{crit}})} \right), \tag{27}$$

where $D$ is the isotropic diffusion constant, $R$ is the radius of the obstacle, $c_0$ is the offset CV of the restitution curve (see Ref. [12] for details), and $T_{\text{crit}}$ and $c_{\text{crit}}$ are the critical pacing period and CV of the waves that are paced with $T_{\text{crit}}$, respectively. Despite the difference in cellular anisotropy, we consider the case for $\Phi = 30^\circ$ and $d_r = 5$ that $D$ can be approximated as the critical diffusion constant $D_{\text{crit}} = 0.65$ cm$^2$/ms [see Fig. 4(c)], $c_0 = 24.6$ cm/s, $T_{\text{crit}} = 82.8$ ms [see Fig. 2(a)], and $c_{\text{crit}} = 14.2$ cm/s. Figure 6(b) compares the approximation by Eq. (27) (black dashed line) and the numerical simulation (red circles). Although Eq. (27) approximates $T_{\text{unp}}$ for larger radii well, it is not able to reproduce the dynamics on small obstacles. Comparison of Eq. (27) in the parameter range that leads to the formation of secondary pinned spiral waves [see the region encircled by a white line in Fig. 6(c)] does not completely describe the dynamics, since larger obstacles involve a different scenario from that considered in Ref. [12].

## IV. DISCUSSION

We have shown that $c_{\text{sin}}$ and $c_{\text{crit}}$ follow a linear relationship. Larger $\Phi$ leads to a decrease in CV [40], but the ratio of $c_{\text{sin}}$ and $c_{\text{crit}}$ is constant and independent of the anisotropy ratio $d_r$ of the medium [see Fig. 2(d)]. Waves that propagate on curved obstacles follow the same linear relationship, whereas the correlation factor $\lambda$ is a function of $d_r$. Since rotating waves encounter variable fiber orientation, which increases the complexity of wave propagation around the obstacle, we introduced the effective diffusion constant $D_{\text{eff}}$, following the general form of an eikonal equation [see Eqs. (25) and (26)] with which we can approximate the dynamics of anchored spiral waves. In this study, for simplicity, only the averaged CV is assumed [see Eq. (21)], although the CV on the obstacle is a function of the local fiber orientation. The knowledge of CV ($d_r$) may also open ways to analyze the dynamics of wave propagation on a round obstacle in anisotropic media by considering an elliptic obstacle in isotropic media.

The termination of pinned spiral waves from nonexcitable obstacles by high-frequency wave trains has been examined experimentally and numerically in various studies that investigated the dynamics in cardiac tissue [8,9,11–13,18,22]. Although the basic mechanism is well understood, the lack of cell anisotropy, a basic feature in a real beating heart, in experimental and numerical models gives a rather unrealistic picture of the actual dynamics in the heart. Cherubini *et al.* [13] recently introduced electroelastic coupling to the model, and elasticity was observed to play a nonprominent role. In contrast, in this study, a significant difference in unpinning

dynamics was found using a model that exhibits cellular fiber orientation. We found that the rotational direction of the spiral wave is significant, since the local fiber orientation plays an essential role in determining the position of the annihilation of the obstacle and, thus, the depinning scenario. Changing the chirality of the pinned spiral leads to a different annihilation position of the spiral wave and, thus, to a different local fiber orientation. To obtain a comparable $R$-$\Phi$ dependence, as shown in Fig. 6(c), the stimulation position has to be changed to the opposite direction toward the obstacle, leading to virtually the same dependences. We found that a nonmonotonic dependence exists between the obstacle radius and the maximum unpinning period depending on the fiber orientation, in contrast to the case with an isotropic excitable medium. Further, for a wide parameter range of obstacle radii and fiber orientation with respect to the approaching waves, the formation of secondary pinned spiral waves was observed, which can also lead to multiarm spiral waves at obstacles, similar to the results observed in cardiac tissue culture [4]. In rare cases, we observed chaotic wave behavior. Thus, if terminating pulses are delivered more transversely with respect to the general fiber direction, they are more likely to initiate new waves or chaotic activity, especially at greater heterogeneities. The latter process of initiating reentrant patterns is reminiscent of earlier findings, where it was shown that if the frequency of stimulation is sufficiently high and the size of the obstacle is sufficiently large, a reentrant pattern can be initiated even without the existence of a pinned spiral wave [6,14].

In this study, we did not address the Zykov limit [44], which describes the CV for curved wavefronts in isotropic excitable media. Although it is possible to calculate the correction factor that may be considered in highly dispersive excitable media, as shown in [41,42], we want to emphasize that the equations that we have introduced here do not explicitly consider the wavefront curvature, but rather consider the curvature of the obstacle along which the waves propagate. Hörning *et al.* have shown that, for certain excitabilities in isotropic medium, the obstacle curvature and the wavefront curvature at the obstacle can be approximated as being equal. However, this may not be the case for tissue that exhibits cellular anisotropy and fiber orientation, and thus further detailed investigations are needed.

Although the results that we obtained in this study show consistent relations with changes in the level of anisotropy, studies on more complex (anisotropic) geometries of different structures, such as in fibers with an abrupt angle change (T-bone) or V-structure, are necessary to provide a full picture of the underlying mechanisms that are present in a real heart. Further, the use of more detailed models such as the Luo Rudy model [45,46] might reveal more complex relationships due to the possibility of complex wave formation [47] and the occurrence of hysteresis and bistable phenomena in periodically paced cardiac tissue due to gap junctional conductance on cell-to-cell propagation [48,49]. Further, different parameter sets should be considered that lead to different wave trajectories and thus may change the underlying dynamics. In this study, we discussed only the case of a circular wave trajectory (see Fig. 1). However, in experiments, linear trajectories are more common [29], and certain trajectories may even lead to reflection of spirals on obstacles [7].

The results reported here indicate that the unpinning of an obstacle-anchored spiral wave in cellular anisotropic excitable media is determined by the curvature effect and the dispersion and restitution properties, as found in previous studies on isotropic excitable media [12,13,50]. The complexity of the response to applied stimuli increases, since an obstacle within an anisotropic medium leads to rotating waves that encounter variable fiber orientations. Thus, the direction of the applied stimuli, the obstacle size, and the rotational direction of the spiral wave on the obstacle play essential roles in determining the depinning scenario, and may influence the outcome of the applied clinical therapy.

## ACKNOWLEDGMENTS

I wish to thank Kenichi Yoshikawa and Tatsuo Shibata for providing the environment that made this research possible. Further, I wish to thank Emilia Entcheva, André Galuschko, and François Blanchard for their helpful comments on the manuscript. This work was supported by the Foreign Postdoctoral Researcher program at RIKEN.

[1] G. Mines, Trans. R. Soc. Can. **4**, 43 (1914).
[2] W. Spinelli and B. Hoffman, Circ. Res. **65**, 1565 (1989).
[3] M. S. Wathen, P. DeGroot, M. Sweeney, A. Stark, M. F. Otterness, W. O. Adkisson, R. C. Canby, K. Khalighi, C. Machado, D. S. Rubenstein *et al.*, Circulation **110**, 2591 (2004).
[4] N. Bursac, F. Aguel, and L. Tung, Proc. Natl. Acad. Sci. (USA) **101**, 15530 (2004).
[5] A. T. Winfree, Science **266**, 1003 (2004).
[6] K. Agladze, J. Keener, S. Muller, and A. Panfilov, Science **264**, 1746 (1994).
[7] D. Olmos, Phys. Rev. E **81**, 041924 (2010).
[8] A. Isomura, M. Hörning, K. Agladze, and K. Yoshikawa, Phys. Rev. E **78**, 066216 (2008).
[9] P. Bittihn, G. Luther, E. Bodenschatz, V. Krinsky, U. Parlitz, and S. Luther, New J. Phys. **10**, 103012 (2008).
[10] M. Tanaka, A. Isomura, M. Hörning, H. Kitahata, K. Agladze, and K. Yoshikawa, Chaos **19**, 043114 (2009).
[11] A. Pumir, S. Sinha, S. Sridhar, M. Argentina, M. Hörning, S. Filippi, C. Cherubini, S. Luther, and V. Krinsky, Phys. Rev. E **81**, 010901(R) (2010).
[12] M. Hörning, A. Isomura, Z. Jia, E. Entcheva, and K. Yoshikawa, Phys. Rev. E **81**, 056202 (2010).
[13] C. Cherubini, S. Filippi, and A. Gizzi, Phys. Rev. E **85**, 031915 (2012).
[14] A. Panfilov and J. Keener, J. Theor. Biol. **163**, 439 (1993).
[15] A. Schaumann, F. von zur Mühlen, B. Herse, B. Gonska, and H. Kreuzer, Circulation **97**, 66 (1998).

[16] G. Lin, A. Dispenzieri, and P. A. Brady, Eur. Heart J. **31**, 1538 (2010).
[17] S. Luther, F. Fenton, B. Kornreich, A. Squires, P. Bittihn, D. Hornung, M. Zabel, J. Flanders, A. Gladuli, L. Campoy *et al.*, Nature (London) **475**, 235 (2011).
[18] S. Takagi, A. Pumir, D. Pazo, I. Efimov, V. Nikolski, and V. Krinsky, Phys. Rev. Lett. **93**, 058101 (2004).
[19] J. Cysyk and L. Tung, Biophys. J. **94**, 1533 (2008).
[20] A. Pumir, V. Nikolski, M. Hörning, A. Isomura, K. Agladze, K. Yoshikawa, R. Gilmour, E. Bodenschatz, and V. Krinsky, Phys. Rev. Lett. **99**, 208101 (2007).
[21] F. Fenton, S. Luther, E. Cherry, N. Otani, V. Krinsky, A. Pumir, E. Bodenschatz, and J. R. F. Gilmour, Circulation **120**, 467 (2009).
[22] C. M. Ripplinger, V. Krinsky, V. Nikolski, and I. Efimov, Am. J. Physiol. **291**, H184 (2006).
[23] M. Hörning, S. Takagi, and K. Yoshikawa, Phys. Rev. E **82**, 021926 (2010).
[24] M. Hörning, S. Takagi, and K. Yoshikawa, Phys. Rev. E **85**, 061906 (2012).
[25] P. Bitthin, M. Hörning, and S. Luther, Phys. Rev. Lett. (to be published).
[26] V. Sidorov, M. Woods, P. Baudenbacher, and F. Baudenbacher, J. Physiol. **289**, 2602 (2005).
[27] R. Clayton, O. Bernus, E. Cherry, H. Dierckx, F. Fenton, L. Mirabella, A. Panfilov, F. Sachse, G. Seemann, and H. Zhang, Prog. Biophys. Molec. Biol. **104**, 22 (2011).
[28] F. Fenton and A. Karma, Chaos **8**, 20 (1998).
[29] F. Fenton, E. Cherry, H. Hastings, and S. Evans, Chaos **12**, 852 (2002).
[30] E. Cherry and F. Fenton, Am. J. Physiol. Heart Circ. **286**, 2332 (2004).
[31] M. Hörning, A. Isomura, K. Agladze, and K. Yoshikawa, Phys. Rev. E **79**, 026218 (2009).
[32] L. Clerc, J. Physiol. **255**, 335 (1976).
[33] D. E. Roberts, L. T. Hersch, and A. M. Scher, Circ. Res. **44**, 701 (1979).
[34] D. E. Roberts and A. M. Scher, Circ. Res. **50**, 342 (1982).
[35] D. W. Peaceman and J. H. H. Rachford, J. Soc. Indust. Appl. Math. **3**, 28 (1955).
[36] F. Fenton, E. Cherry, A. Karma, and W. Rappel, Chaos **15**, 013502 (2005).
[37] Z. Jia, H. Bien, Y. Shiferaw, and E. Entcheva, Biophys. J. **102**, 1294 (2012).
[38] E. G. Tolkacheva and X. Zhao, Nonlin. Dyn. **68**, 347 (2012).
[39] H. Bien, L. Yin, and E. Entcheva, Biophys. J. **90**, 2628 (2006).
[40] J. Keener and J. Sneyd, *Mathematical Physiology*, 2nd edition, Vol. XXV (Springer, New York, 2009).
[41] V. Fast and A. Kleber, Cardiovasc. Res. **33**, 258 (1996).
[42] A. M. Pertsov, M. Wellner, and J. Jalife, Phys. Rev. Lett. **78**, 2656 (1997).
[43] L. Glass, Science **198**, 321 (1977).
[44] V. Zykov and O. Morozova, Biophysics **24**, 739 (1979).
[45] C. Luo and Y. Rudy, Circ. Res. **68**, 1501 (1991).
[46] C. Luo and Y. Rudy, Circ. Res. **74**, 1071 (1994).
[47] S. Alonso and A. Panfilov, Phys. Rev. Lett. **100**, 218101 (2008).
[48] A. Kleber and Y. Rudy, Physiol. Rev. **84**, 431 (2004).
[49] X. Huang, Y. Qian, X. Zhang, and G. Hu, Phys. Rev. E **81**, 051903 (2010).
[50] V. Zykov, G. Bordyugovb, H. Lentz, and H. Engel, Physica D **239**, 797 (2010).